



THE UNIVERSITY *of* EDINBURGH

Edinburgh Research Explorer

Constraining human contributions to observed warming since the pre-industrial period

Citation for published version:

Gillett, NP, Kirchmeier-young, M, Ribes, A, Shiogama, H, Hegerl, GC, Knutti, R, Gastineau, G, John, JG, Li, L, Nazarenko, L, Rosenbloom, N, Seland, Ø, Wu, T, Yukimoto, S & Ziehn, T 2021, 'Constraining human contributions to observed warming since the pre-industrial period', *Nature Climate Change*.
<https://doi.org/10.1038/s41558-020-00965-9>

Digital Object Identifier (DOI):

[10.1038/s41558-020-00965-9](https://doi.org/10.1038/s41558-020-00965-9)

Link:

[Link to publication record in Edinburgh Research Explorer](#)

Document Version:

Peer reviewed version

Published In:

Nature Climate Change

General rights

Copyright for the publications made accessible via the Edinburgh Research Explorer is retained by the author(s) and / or other copyright owners and it is a condition of accessing these publications that users recognise and abide by the legal requirements associated with these rights.

Take down policy

The University of Edinburgh has made every reasonable effort to ensure that Edinburgh Research Explorer content complies with UK legislation. If you believe that the public display of this file breaches copyright please contact openaccess@ed.ac.uk providing details, and we will remove access to the work immediately and investigate your claim.



1 **Constraining human contributions to observed warming since preindustrial**

2 Nathan P. Gillett¹, Megan Kirchmeier-Young², Aurélien Ribes³, Hideo Shiogama⁴, Gabi Hegerl⁵,
3 Reto Knutti⁶, Guillaume Gastineau⁷, Jasmin G. John⁸, Lijuan Li⁹, Larissa Nazarenko¹⁰, Nan
4 Rosenbloom¹¹, Øyvind Seland¹², Tongwen Wu¹³, Seiji Yukimoto¹⁴, Tilo Ziehn¹⁵

5
6 ¹Canadian Centre for Climate Modelling and Analysis, Environment and Climate Change
7 Canada, Victoria, BC, Canada.

8 ²Climate Research Division, Environment and Climate Change Canada, Toronto, ON, Canada.

9 ³CNRM, Université de Toulouse, Météo-France, CNRS, Toulouse, France.

10 ⁴Center for Global Environmental Research, National Institute for Environmental Studies, Tsukuba,
11 Japan.

12 ⁵University of Edinburgh, School of Geosciences, Edinburgh, United Kingdom.

13 ⁶ETH Zurich, Institute for Atmospheric and Climate Science, Zurich, Switzerland.

14 ⁷LOCEAN/Institut Pierre Simon Laplace, Paris, France.

15 ⁸NOAA/OAR/Geophysical Fluid Dynamics Laboratory, Princeton, NJ, USA.

16 ⁹LASG, Institute of Atmospheric Physics, Beijing, China.

17 ¹⁰NASA Goddard Institute for Space Studies, New York, NY, USA.

18 ¹¹NCAR, Boulder, CO, USA.

19 ¹²Norwegian Meteorological Institute, Oslo, Norway.

20 ¹³Beijing Climate Center, China Meteorological Administration, Beijing, China.

21 ¹⁴Meteorological Research Institute, Tsukuba, Japan.

22 ¹⁵CSIRO Oceans and Atmosphere, Aspendale, Victoria, Australia.

23
24 **Parties to the Paris Agreement agreed to holding global average temperature increases**
25 **'well below 2 °C above pre-industrial levels' and 'pursuing efforts to limit the temperature**
26 **increase to 1.5 °C above pre-industrial levels'. Monitoring the contributions of human-**
27 **induced climate forcings to warming to date is key to understanding progress towards**
28 **these goals. Here we use climate model simulations from the Detection and Attribution**
29 **Model Intercomparison Project (DAMIP), as well as regularised optimal fingerprinting**
30 **(ROF), to estimate that anthropogenic forcings caused 0.9–1.3 °C of warming in global**
31 **mean near-surface air temperature in 2010–2019 relative to 1850–1900, compared to an**
32 **observed warming of 1.1 °C, with greenhouse gases and aerosols contributing changes of**
33 **1.2 – 1.9 °C and -0.7 – -0.1 °C, respectively, and natural forcings contributing negligibly.**
34 **These results demonstrate the substantial human influence on climate to date and the**
35 **urgency of action needed to meet the Paris Agreement goals.**

36
37 For more than twenty years, detection and attribution techniques have been used to identify
38 human influence in global temperature changes, and to quantify the contributions of individual
39 forcings to observed changes^{1–3}. The commitment of parties to the Paris Agreement⁴ to ‘holding
40 the increase in the global average temperature to well below 2 °C above pre-industrial levels, and

pursuing efforts to limit the temperature increase to 1.5 °C above pre-industrial levels’, and the Global Stocktake process which aims to monitor progress towards the Paris goals, give new relevance to efforts to quantify human climate influence to date. While the Paris Agreement is not explicit about the meaning of either ‘global average temperature’ or ‘pre-industrial levels’, much of the climate impacts literature on which assessment of dangerous anthropogenic interference in climate is based has used globally-complete global mean near-surface air temperature (GSAT) from climate models to assess future climate impacts. Therefore we primarily assess human influence on GSAT here. Recent literature demonstrates that in climate models this metric of global mean temperature warms more than blended sea surface temperatures over ocean and near-surface air temperature over land, masked with observational coverage (GMST)^{5–7}. Previous attribution studies typically estimated attributable trends over the past 50–60 years in GMST⁸, but estimates of warming relative to pre-industrial levels are more relevant to monitoring progress towards Paris Agreement goals. While multiple possible periods over the Holocene could be chosen as pre-industrial base periods⁹, we follow the IPCC Special Report on 1.5 °C¹⁰ (SR1.5) and choose 1850–1900.

Comparison of global mean temperature metrics

Annual mean global mean temperature anomalies in the HadCRUT4¹¹ dataset, relative to 1850–1900, based on an area-weighted global mean of monthly-mean anomalies are shown in Figure 1a. These are compared with global mean blended sea surface temperature over ocean and near surface air temperature over land and ice masked with HadCRUT4 coverage⁵ (GMST, see Methods) in individual CMIP6¹² historical simulations merged with SSP2-4.5¹³ simulations (historical-ssp245 simulations hereafter). The simulated warming in 2010–2019 is 17% (5–95% range of 10%–24%) stronger in globally-complete GSAT than in HadCRUT4-masked GMST (Figure 1a), similar to previous results based on CMIP5^{14,15}, demonstrating the importance of the choice of metric for assessing attributable warming. Comparing globally-complete versions of GSAT and GMST, the simulated warming in GSAT is only 6% stronger (5–95% range of 2%–8%). Hence the largest contribution to the enhanced warming in globally-complete GSAT versus HadCRUT4-masked GMST warming comes from the observational masking.

Multiplying the observed 2010–2019 warming in HadCRUT4 GMST of 0.94 °C (5–95% range of 0.90–0.99 °C, see Supplementary Table 1), by the ratio of simulated warming in globally-complete GSAT to HadCRUT4-masked GMST (1.17), we infer a best estimate of observed 2010–2019 warming in GSAT of 1.10 °C (5–95% range of 1.01–1.20 °C). Similar calculations using GISTEMP¹⁶ and NOAA GlobalTemp¹⁷ yield estimates of observed GSAT warming in 2010–2019 of 1.18 °C and 1.12 °C respectively (Supplementary Table 1). For the remainder of the study we primarily report results based on the non-infilled HadCRUT4 dataset, and to ensure a like-for-like comparison, we use masked and blended model output when comparing with

HadCRUT4 observations, including in all regressions. However, we report attributable warming based on simulated globally-complete GSAT.

Attribution of global mean temperature changes

In order to quantify the contributions of individual forcings to observed trends we used the CMIP6¹² DAMIP¹⁸ simulations from the thirteen CMIP6 models for which the necessary simulations were available (Figure 1b, Extended Data Figure 1, Supplementary Table 2): ACCESS-ESM1-5¹⁹, BCC-CSM2-MR²⁰, CanESM5²¹, CESM2²², CNRM-CM6-1²³, FGOALS-g3²⁴, GFDL-ESM4²⁵, GISS-E2-1-G²⁶, HadGEM3-GC31-LL²⁷, IPSL-CM6A-LR²⁸, MIROC6²⁹, MRI-ESM2-0³⁰ and NorESM2-LM³¹. We primarily used output from four experiments: historical-ssp245 (driven with changes in all anthropogenic and natural forcings), hist-aer (driven with changes in anthropogenic aerosol emissions and burdens only), hist-nat (driven with changes in natural forcings only), and hist-GHG (driven with changes in well-mixed greenhouse gas concentrations only). The CMIP6 historical-ssp245 simulations show very little net anthropogenic warming prior to the 1960s (Figure 1b). This is in contrast to the CMIP5 historical simulations, which showed on average approximately 0.2 °C warming by the mid-20th century⁸. This could be due in part to a stronger aerosol forcing or response in these CMIP6 models. If these CMIP6 simulations are correct, this would imply that there was very little net anthropogenic contribution to the early 20th century warming, and that almost all anthropogenic warming has occurred since the 1960s. We use global mean temperature in our main attribution analysis, since previous work^{7,32} has shown that including more spatial detail may not result in more robust results, perhaps because model uncertainty in spatial patterns of response is larger. We use five-year means rather than decadal means^{32,33}, in an attempt to better constrain the natural forcing response, which includes the short timescale response to volcanic eruptions. Internal variability was estimated from intra-ensemble anomalies (see Methods).

Regression coefficients of observed temperature changes against individual models' simulated response to natural and anthropogenic forcings are shown in Figure 2a (see Methods). The anthropogenic response is detected using twelve of thirteen models (the uncertainty ranges on the ANT regression coefficients are above zero). The only exception is ACCESS-ESM1-5, which exhibits apparently unrealistic GMST evolution in its historical simulations, with almost no warming prior to 1980¹⁹ (Figure 1a). By contrast, the natural forcing response is only detected using CanESM5, CESM2, CNRM-CM6-1, FGOALS-g3 and IPSL-CM6A-LR, and its regression coefficient is significantly less than unity using eight of the thirteen models, meaning that the simulated NAT response in these models is significantly stronger than observed. The natural forcing response appears to be somewhat less detectable and consistent based on these CMIP6 simulations than using CMIP5 simulations^{8,32–34}. Based on this regression the combined anthropogenic response is of realistic magnitude in ACCESS-ESM1-5, BCC-CSM2-MR, CESM2, CNRM-CM6-1, FGOALS-g3, GISS-E2-1-G, HadGEM3-GC31-LL, IPSL-CM6A-LR

and NorESM2-LM, significantly overestimated by CanESM5²¹, which is also apparent from Figure 1a, and significantly underestimated by GFDL-ESM4, MIROC6 and MRI-ESM2-0. Note that it is to be expected that significant differences between the simulated climate response in models and observations can increasingly be identified as the observational record lengthens.

The realism of the scaled simulated responses to each set of forcings can be assessed by comparing residual observed variability, after subtraction of these responses, with simulated internal variability. The results of a residual consistency test^{32,35} (Figure 2c) indicate that residuals are inconsistent with pooled simulated internal variability for ACCESS-ESM1-5, CanESM5, CESM2, GISS-E2-1-G, HadGEM3-GC31-LL and NorESM2-LM, for which the residual is significantly larger than expected at the 5% level, and similar results were obtained for a three-way regression (Figure 2d). This could be related to the cool temperatures through the mid-20th century simulated in the historical simulations of these models, with little warming apparent before 1975 (Figure 1a).

In order to quantify the separate contributions of greenhouse gases and aerosols to observed changes, we show the results of a three-way regression onto the simulated responses to aerosols (AER, inferred from hist-aer), natural forcings (NAT, inferred from hist-nat), and greenhouse gases (GHG, inferred from historical-ssp245 minus hist-aer minus hist-nat, and including the response to well-mixed greenhouse gases, ozone and land-use change) in Figure 2b. The GHG response is detected using eleven of thirteen models, and the AER and NAT responses are detected using six. Our results suggest that ACCESS-ESM1-5, CanESM5, CESM2 and HadGEM3-GC31-LL significantly overestimate the responses to both greenhouse gases and aerosols, and that FGOALS-g3 underestimates them. NorESM2-LM appears to overestimate the response to aerosols, while MIROC6 and MRI-ESM2-0 underestimate the response to greenhouse gases. Regression coefficients from the three-way regression are poorly constrained in the case of GFDL-ESM4, which may be because its hist-aer ensemble has only a single ensemble member (Supplementary Table 2). Attributable temperature changes in 2010–2019 from the two-way regression (Figure 2e) are generally consistent between the models, albeit with differences in the width of the uncertainty ranges, while individual model attributable temperature changes based on the three-way regression are in some cases inconsistent between models, which may reflect the effects of model uncertainty, which is not accounted here. Results obtained based on a three-way regression of the observations onto the simulated response to aerosols and other anthropogenic forcings (inferred from historical-ssp245 minus hist-GHG minus hist-nat, and including the response to aerosols, ozone and land-use change), natural forcings (from hist-nat), and well-mixed greenhouse gases (from hist-GHG) are less well-constrained and show larger differences between models (Extended Data Figure 2), which may be partly because in this case the weaker aerosol response is estimated from the noisy residual, rather than the stronger greenhouse-gas response³⁴.

In addition to results based on individual model response patterns, we also present results based on an average of responses across models, using all available ensemble members, but giving equal weight to each model^{7,33,34}. Since the ROF method does not explicitly account for model uncertainty, and previous work has shown that using the multi-model mean could lead to overconfident results⁷, we first evaluate the multi-model mean approach in an imperfect model framework^{7,32,36}. We withhold one of the thirteen models from the multi-model average, treat one of its historical-ssp245 simulations as pseudo-observations, and use the remaining twelve models in a multi-model analysis to calculate the best estimate and 5–95% confidence interval on its GHG, AER and NAT response in globally-complete GSAT (Figure 3, y-axis), which can be compared with the true ensemble-mean simulated value in that model (Figure 3, x-axis). The process is repeated for all 105 historical-ssp245 simulations. The percentages of reconstructed attributable changes consistent with the true simulated changes at the 10% level were 91%, 90% and 79% for GHG, AER, and NAT respectively. These percentages are close to the expected 90% coverage ratio, particularly for GHG and AER. These results suggest that under the paradigm that these models are statistically indistinguishable from the truth³⁷, the confidence intervals for aerosol and greenhouse gas attributable changes are robust.

Using a multi-model average of all thirteen models, we find a detectable response to anthropogenic forcing in a two-way regression, and a detectable response to GHG and AER in a three-way regression, with regression coefficients consistent with one and more closely constrained than based on most, though not all, individual model analyses (Figures 2a and b). However, the NAT response was not detected. We find 0.9–1.3 °C (5–95% range) of warming in GSAT in 2010–2019 relative to 1850–1900 attributable to anthropogenic forcings, consistent with our estimate of observed warming of 1.10 °C, with GHG, AER and NAT forcings contributing changes of 1.2 – 1.9 °C, -0.7 – -0.1 °C and -0.01 – 0.06 °C respectively (Table 1). We find consistent residuals (Figures 2c and d), and anthropogenic-attributable warming ranges which differ by no more than 0.12 °C when using either GISTEMP or NOAA GlobalTemp in place of HadCRUT4 (Extended Data Figures 3 and 4, Table 1), or when using hemispheric means in place of global means (Extended Data Figure 5, Table 1). Considered together with the imperfect model test, these results give us confidence that our multi-model estimates of attributable changes in temperature are robust. As expected, multi-model estimates of GHG-attributable warming and AER-attributable cooling are both somewhat smaller in magnitude when the effects of ozone are grouped with those of aerosols rather than GHGs (Extended Data Figure 2, Table 1). Our estimated 5–95% range of anthropogenic-attributable warming in GMST in 2010–2019 of 0.8 – 1.1 °C (Table 1) is consistent with the assessed likely range of anthropogenic warming of 0.8 – 1.2 °C in 2017 in SR1.5¹⁴. This was based in part on a study which regressed HadCRUT4 GMST onto the simulated anthropogenic response from an impulse-response function model and obtained a 5–95% range of anthropogenic warming in 2017 of 0.87–1.22 °C³⁸.

As well as informing us about the contributions of different forcings to observed climate change, information from detection and attribution analyses can also tell us about the degree of realism of climate models and whether they overpredict or underpredict the responses to particular forcings. Such information is useful for interpreting projections from these models. Much attention has recently focused on the high climate sensitivity of some CMIP6 models³⁹, and while we find that some of the models considered here do overestimate the response to greenhouse gases, on average the greenhouse gas response of these models matches the observations closely (the best estimate of the multi-model greenhouse gas regression coefficient in Figure 2b is close to one). By contrast, while the multi-model mean aerosol response is not inconsistent with the observations, the best estimate is that these models overestimate the response to aerosols by about 30% (the best estimate of the multi-model aerosol regression coefficient in Figure 2b is 0.76). Given that future climate change is expected to be dominated by greenhouse gas changes, overall these results increase confidence in the ensemble mean magnitude of projected warming derived from these models. At the same time, the significant differences in response between some models and observations identified here, are consistent with the finding that observational constraints may be used to narrow the uncertainty range of projected warming based on CMIP6 models^{40,41}.

Estimates of greenhouse gas and aerosol-attributable warming relative to preindustrial have not been previously published, but it is notable that our estimated contributions from these forcings of 1.2 – 1.9 °C and -0.7 – -0.1 °C are substantially larger for example than their assessed likely contributions to 1951–2010 trends in GMST of 0.5 – 1.4 °C and -0.5 – 0.1 °C respectively in AR5⁸. This is probably due to our consideration of a longer period starting in 1850 and ending in 2019, our use of GSAT rather than GMST, and our grouping of ozone with well-mixed greenhouse gases, rather than with aerosols. Nonetheless, we suggest that our results give a fairer picture of the very substantial, albeit partly compensating, influences of human-induced changes in greenhouse gases and aerosols to date. While the Paris Agreement⁴ is not explicit on whether the ‘increase in the global average temperature’ it describes is in GMST or GSAT, nor what the appropriate definition of preindustrial is, nor whether it is referring to anthropogenic warming or total warming, our analysis suggests anthropogenic warming may already be close to the 1.5 °C threshold.

Methods

We downloaded monthly mean near-surface air temperature (tas), sea surface temperature (tos), and sea ice concentration (siconc) from all the CMIP6 models for which the necessary CMIP6 historical¹², ScenarioMIP¹³ SSP2-4.5 and DAMIP¹⁸ hist-nat and hist-aer simulations were available (Supplementary Table 2). SSP2-4.5 forcings were used in the DAMIP simulations for the 2015–2020 period¹⁸, so we merged CMIP6 historical simulations with SSP2-4.5 simulations for the period 2015–2019 for consistency. We used ESMValTool⁴² to preprocess the model output, and used Cowtan⁵ code to calculate masked and blended temperature from the model output using HadCRUT4¹¹ observational masking, and using anomalies and variable sea ice concentration⁵. We calculated 5-year mean global means of these data using area-weighting, for the period January 1850 to December 2019 to give a vector with 34 elements, and then subtracted the long-term mean to give anomalies. Due to limited availability of the land-sea mask from some models, the land-sea mask from CNRM-CM6-1, regridded onto a 5°×5° grid, was used for all models.

Observed GMST was calculated from HadCRUT4¹¹ monthly anomalies by area weighting, taking 5-year means, and subtracting the long-term mean to give anomalies. The median dataset was used for the main analysis results, and each of the 100 members of the ensemble dataset were treated in the same way and used to derive uncertainties in the multi-model attributable warming estimates (see also Extended Data Figure 6). The uncertainty range in inferred observed GSAT warming was obtained by randomly sampling a HadCRUT4 ensemble member, and the ratio of GSAT to GMST warming from an individual historical-ssp245 simulation, taking the product, and repeating 10000 times, with equal weight given to each CMIP6 model. The NOAAGlobalTemp¹⁷ (v5) dataset starts in 1880, but our analysis required data from 1850, so we concatenated HadCRUT4 anomalies relative to the NOAAGlobalTemp 1971–2000 base period over the 1850–1879 period with NOAAGlobalTemp, and then calculated global mean 5-yr mean anomalies as for HadCRUT4. The GISTEMP¹⁶ (v4) data are available on a 2°×2° grid, so we first interpolated onto the HadCRUT4 5°×5° grid. We then concatenated with HadCRUT4 anomalies relative to the GISTEMP base period of 1951–1980 over the period 1850–1879, since GISTEMP starts in 1880. We then calculated global-mean 5-yr anomalies as for the other datasets. Five-year mean hemispheric means (Extended Data Figure 5) were calculated in the same way from gridded anomalies in masked and blended model output and observations.

An optimal detection analysis was performed using the Regularised Optimal Fingerprinting algorithm^{32,35}, implemented in Python⁴³. This technique is a variant of linear regression, in which

the time-series of observed GMST changes Y is regressed onto the simulated responses to sets of forcings X_i , i.e.

$$Y = \sum \beta_i X_i + \epsilon,$$

where ϵ denotes internal variability. A total least squares algorithm was used to account for noise in the regressors X_i , i.e. the fact that simulated responses to forcings are affected by internal variability (due to small ensemble sizes)³⁵. Key detection and attribution diagnoses were derived from the inferred scaling factors β_i . The response to forcing i is detected if β_i is significantly non-zero. Attribution further requires β_i being consistent with unity (i.e., consistency between the observed and simulated responses). Optimal estimation within this statistical model requires an estimate of the covariance matrix of ϵ , Σ , which is estimated from a sample of internal variability realisations simulated by the available climate models. Realisations of internal variability were calculated from all available ensembles of size greater than one (Supplementary Table 2), by subtracting the ensemble mean, and then inflating anomalies by $\sqrt{\frac{N}{N-1}}$ where N is the ensemble size, to account for the subtraction of the ensemble mean. Note that some of the models included here, particularly BCC-CSM2-MR, CNRM-CM6-1 and IPSL-CM6A-LR, have very high internal variability⁴⁴, which will tend to inflate uncertainties compared to similar studies performed using CMIP5⁸. For an ensemble of size N , $N-1$ anomaly segments were calculated, since the N^{th} sample calculated in this way is a linear combination of the other $N-1$ segments. This gave rise to 478 realisations of internal variability, which were used in all attribution analyses shown in this study. After pooling realisations across simulation type and model, half of these realisations (239 realisations, which is much more than the size of our detection vector), sampled alternately, were used to estimate the covariance matrix of internal variability for optimization, and the remaining half were used for the residual consistency test. All analyses were performed using a multi-model mean estimate of internal variability. The main analyses presented used historical-ssp245 and hist-nat simulations for the two-way regressions, and historical-ssp245, hist-nat, and hist-aer simulations¹⁸ for the three way regressions. Regression coefficients corresponding to natural forcings, greenhouse gases and aerosols were then calculated from these regression coefficients², and are shown in Figures 2a and b.

Estimates of attributable warming in GSAT in 2010–2019 were calculated by multiplying these regression coefficients by the corresponding ensemble mean globally-complete GSAT response in 2010–2019 to each of the forcings concerned, with the anthropogenic response inferred by subtracting hist-nat from historical-ssp245 and the GHG response inferred by subtracting hist-aer and hist-nat from historical-ssp245. Since uncertainty in the attributable warming arises both from uncertainties in the regression coefficients and uncertainties in the ensemble mean simulated response to each forcing due to internal variability, we added uncertainty components from the regression coefficient and ensemble mean simulated warming in quadrature, treating positive and negative departures from the best estimate separately, to allow for skewness in the distribution of the regression coefficients. This approach is valid under the assumption that the

uncertainties in the regression coefficients and the uncertainty in the simulated warming in 2010–2019 are Gaussian, uncorrelated and small compared to their respective means, though as noted we do make a first order correction for non-Gaussian regression coefficient distributions by treating positive and negative departures separately.

Since the ratio of warming in GSAT to HadCRUT4-masked GMST varies between models (Extended Data Figure 7), in the multi-model analysis we added an uncertainty contribution based on the spread in this ratio across models in place of the contribution from internal variability in the ensemble mean response to each forcing in an individual model. Further in the multi-model analyses based on HadCRUT4, we added an additional uncertainty component to account for observational uncertainty, based on the spread in regression coefficients across the 100-member HadCRUT4 ensemble (Extended Data Figure 6). These contributions were added in quadrature to the uncertainties arising from the uncertainty in the regression coefficients, in the same way as described for individual models in the previous paragraph. Attributable warming ranges calculated in this way were very similar to those calculated based only on the uncertainty in the regression coefficient in the multi-model analysis and for models with large ensembles, and exhibited somewhat larger ranges for most models with smaller ensemble sizes (Extended Data Figure 8), and substantially larger ranges for BCC-CSM2-MR due to its small ensemble sizes (Supplementary Table 2) and large internal variability⁴⁴. For the multi-model analyses, response patterns for each forcing were calculated by averaging individual response patterns over the thirteen models used (Supplementary Table 2). Individual response patterns were averaged with equal weight given to each model, and the corresponding effective ensemble size was calculated and used in the analysis. Attributable changes in GMST (Table 1) were calculated in the same way as for globally-complete GSAT, but used HadCRUT4-masked GMST from the models in place of globally-complete GSAT.

The imperfect model test was carried out by withholding one model at a time from the multi-model analysis, and using each of its historical-ssp245 simulations in turn as pseudo-observations. Masked and blended temperatures (using the HadCRUT4 observational mask) from this simulation were then treated as observations, and a multi-model analysis using the remaining twelve models was used to infer that model's ensemble mean 2010–2019 warming in response to natural forcings, greenhouse gases and aerosols, and associated 5–95% confidence ranges, using the same approach as that used to derive the multi-model results presented in Figure 2. Uncertainties in the attributable warming calculation were calculated as in the main analysis, and uncertainties in the ensemble mean response to each forcing (shown on the *x*-axis of Figure 3), were additionally accounted for when assessing consistency.

343 Acknowledgements

344 We thank Daithi Stone, Nicolas Bellouin, Sun Ying and Mike Winton for helpful comments on
345 the analysis and manuscript, and Lisa Bock for assistance with ESMValTool. We acknowledge
346 the World Climate Research Programme, which, through its Working Group on Coupled
347 Modelling, coordinated and promoted CMIP6, and the modelling groups whose output we use.
348

349 Author contributions

350 NPG carried out the analysis and led writing of the manuscript. MKY developed the Python code
351 used in the attribution analysis. AR developed the algorithm used in the analysis. All coauthors
352 advised on the analysis and contributed to drafting the manuscript.
353

354 Competing interests

355 The authors declare no competing interests.
356

357 Data availability

358 All figures in this manuscript use CMIP6 data available here ([https://esgf-](https://esgf-node.llnl.gov/projects/cmip6/)
359 [node.llnl.gov/projects/cmip6/](https://esgf-node.llnl.gov/projects/cmip6/)). The DOIs of the CMIP6 datasets used from each model were:
360 ACCESS-ESM1-5: 10.22033/ESGF/CMIP6.2288, 10.22033/ESGF/CMIP6.14362,
361 10.22033/ESGF/CMIP6.2291; BCC-CSM2-MR: 10.22033/ESGF/CMIP6.1725,
362 10.22033/ESGF/CMIP6.1726, 10.22033/ESGF/CMIP6.1732; CanESM5:
363 10.22033/ESGF/CMIP6.1303, 10.22033/ESGF/CMIP6.1305, 10.22033/ESGF/CMIP6.1317;
364 CESM2: 10.22033/ESGF/CMIP6.2185, 10.22033/ESGF/CMIP6.2187,
365 10.22033/ESGF/CMIP6.2201; CNRM-CM6-1: 10.22033/ESGF/CMIP6.1375,
366 10.22033/ESGF/CMIP6.1376, 10.22033/ESGF/CMIP6.1384; FGOALS-g3:
367 10.22033/ESGF/CMIP6.1783, 10.22033/ESGF/CMIP6.2048, 10.22033/ESGF/CMIP6.2056;
368 GFDL-ESM4: 10.22033/ESGF/CMIP6.1407, 10.22033/ESGF/CMIP6.1408,
369 10.22033/ESGF/CMIP6.1414; GISS-E2-1-G: 10.22033/ESGF/CMIP6.1400,
370 10.22033/ESGF/CMIP6.2062, 10.22033/ESGF/CMIP6.2074; HadGEM3-GC31-LL:
371 10.22033/ESGF/CMIP6.419, 10.22033/ESGF/CMIP6.471, 10.22033/ESGF/CMIP6.10845;
372 IPSL-CM6A-LR: 10.22033/ESGF/CMIP6.1534, 10.22033/ESGF/CMIP6.13801,
373 10.22033/ESGF/CMIP6.1532; MIROC6: 10.22033/ESGF/CMIP6.881,
374 10.22033/ESGF/CMIP6.894, 10.22033/ESGF/CMIP6.898; MRI-ESM2-0:
375 10.22033/ESGF/CMIP6.621, 10.22033/ESGF/CMIP6.634, 10.22033/ESGF/CMIP6.638;
376 NorESM2-LM: 10.22033/ESGF/CMIP6.502, 10.22033/ESGF/CMIP6.580,
377 10.22033/ESGF/CMIP6.604. HadCRUT4 data (version 4.6.0.0 downloaded March 24th 2020)
378 are available here (<https://www.metoffice.gov.uk/hadobs/hadcrut4/>), GISTEMP data (version 4

with 1200-km smoothing, downloaded April 13th 2020) are available here (<https://data.giss.nasa.gov/gistemp/>), and NOAA GlobalTemp data (version 5.0.0 downloaded April 13th 2020) are available here (<https://www.ncdc.noaa.gov/noaa-merged-land-ocean-global-surface-temperature-analysis-noaaglobaltemp-v5>).

Code availability

The analysis code used in this study is based on ESMValTool and is available here (<https://github.com/ESMValGroup/ESMValTool/tree/gillett20>).

Additional information

Correspondence and requests for materials should be addressed to N.P.G.

References

1. Stott, P. A. & Tett, S. F. B. Scale-dependent detection of climate change. *J. Clim.* **11**, 3282–3294 (1998).
2. Allen, M. R. & Tett, S. F. B. Checking for model consistency in optimal fingerprinting. *Clim. Dyn.* **15**, 419–434 (1999).
3. Hegerl, G. C. *et al.* Multi-fingerprint detection and attribution analysis of greenhouse gas, greenhouse gas-plus-aerosol and solar forced climate change. *Clim. Dyn.* **13**, 613–634 (1997).
4. *Paris Agreement*. (United Nations, 2015).
5. Cowtan, K. *et al.* Robust comparison of climate models with observations using blended land air and ocean sea surface temperatures. **42**, 6526–6535 (2015).
6. Richardson, M., Cowtan, K. & Millar, R. J. Global temperature definition affects achievement of long-term climate goals. *Environ. Res. Lett.* **13**, (2018).
7. Schurer, A. *et al.* Estimating the Transient Climate Response from Observed Warming. *J. Clim.* **31**, 8645–8663 (2018).
8. Bindoff, N. L. *et al.* Detection and attribution of climate change: From global to regional. in *Climate Change 2013 the Physical Science Basis: Working Group I Contribution to the Fifth Assessment Report of the Intergovernmental Panel on Climate Change* (eds. Stocker, T. F., Qin, D., Pattner, G.-K., Tignor, M. & Allen) vol. 9781107057 867–952 (Cambridge University Press, 2013).
9. Schurer, A. P., Mann, M. E., Hawkins, E., Tett, S. F. B. & Hegerl, G. C. Importance of the pre-industrial baseline for likelihood of exceeding Paris goals. *Nat. Clim. Chang.* **7**, 563–567 (2017).
10. Masson-Delmotte, V. *et al.* *Global warming of 1.5°C An IPCC Special Report. Report of the Intergovernmental Panel on Climate Change* (2018).
11. Morice, C. P., Kennedy, J. J., Rayner, N. A. & Jones, P. D. Quantifying uncertainties in global and regional temperature change using an ensemble of observational estimates: The HadCRUT4 data set. *J. Geophys. Res. Atmos.* (2012) doi:10.1029/2011JD017187.
12. Eyring, V. *et al.* Overview of the Coupled Model Intercomparison Project Phase 6 (CMIP6) experimental design and organization. *Geosci. Model Dev.* **9**, 1937–1958 (2016).
13. O'Neill, B. C. *et al.* The Scenario Model Intercomparison Project (ScenarioMIP) for

- CMIP6. *Geosci. Model Dev.* (2016) doi:10.5194/gmd-9-3461-2016.
14. Allen, M. R. *et al.* *IPCC: Framing and Context. Global warming of 1.5°C. An IPCC Special Report* (2018).
15. Rogelj, J., Forster, P. M., Kriegler, E., Smith, C. J. & Séférian, R. Estimating and tracking the remaining carbon budget for stringent climate targets. *Nature* **571**, 335–342 (2019).
16. Lenssen, N. J. L. *et al.* Improvements in the GISTEMP Uncertainty Model. *J. Geophys. Res. Atmos.* **124**, 6307–6326 (2019).
17. Huang, B. *et al.* Uncertainty estimates for sea surface temperature and land surface air temperature in NOAA GlobalTemp version 5. *J. Clim.* **33**, 1351–1379 (2020).
18. Gillett, N. P. *et al.* The Detection and Attribution Model Intercomparison Project (DAMIP~v1.0) contribution to CMIP6. *Geosci. Model Dev.* **9**, 3685–3697 (2016).
19. Ziehn, T. *et al.* The Australian Earth System Model: ACCESS-ESM1.5. *J. South. Hemisph. Earth Syst. Sci.* (2020) doi:10.1071/es19035.
20. Wu, T. *et al.* The Beijing Climate Center Climate System Model (BCC-CSM): The main progress from CMIP5 to CMIP6. *Geosci. Model Dev.* (2019) doi:10.5194/gmd-12-1573-2019.
21. Swart, N. C. *et al.* The Canadian Earth System Model version 5 (CanESM5.0.3). *Geosci. Model Dev. Discuss.* (2019) doi:10.5194/gmd-2019-177.
22. Danabasoglu, G. *et al.* The Community Earth System Model Version 2 (CESM2). *J. Adv. Model. Earth Syst.* (2020) doi:10.1029/2019MS001916.
23. Voldoire, A. *et al.* Evaluation of CMIP6 DECK Experiments With CNRM-CM6-1. *J. Adv. Model. Earth Syst.* (2019) doi:10.1029/2019MS001683.
24. Li, L. J. *et al.* The Flexible Global Ocean–Atmosphere–Land System Model Grid-Point Version 3 (FGOALS-g3): Description and Evaluation. *J. Adv. Model. Earth Syst.* (2020) doi:10.1029/2019MS002012.
25. Dunne, J. P. *et al.* The GFDL Earth System Model version 4.1 (GFDL-ESM4.1): Overall coupled model description and simulation characteristics. *J. Adv. Model. Earth Syst.* (2020) doi:10.1029/2019MS002015.
26. Kelley, M. *et al.* GISS-E2.1: Configurations and Climatology. *J. Adv. Model. Earth Syst.* (2020) doi:10.1029/2019MS002025.
27. Williams, K. D. *et al.* The Met Office Global Coupled Model 3.0 and 3.1 (GC3.0 and GC3.1) Configurations. *J. Adv. Model. Earth Syst.* (2018) doi:10.1002/2017MS001115.
28. Boucher, O., Servonnat, J., Albright, A. L., Aumont, O. & Balkanski, Y. Presentation and evaluation of the IPSL-CM6A-LR climate model. *J. Adv. Model. Earth Syst.* (2020) doi:10.1029/2019MS002010.
29. Tatebe, H. *et al.* Description and basic evaluation of simulated mean state, internal variability, and climate sensitivity in MIROC6. *Geosci. Model Dev.* (2019) doi:10.5194/gmd-12-2727-2019.
30. Yukimoto, S. *et al.* The Meteorological Research Institute Earth system model version 2.0, MRI-ESM2.0: Description and basic evaluation of the physical component. *J. Meteorol. Soc. Japan* **97**, 931–965 (2019).
31. Seland, Ø. *et al.* The Norwegian Earth System Model, NorESM2 – Evaluation of the CMIP6 DECK and historical simulations. *Geosci. Model Dev. Discuss.* (2020) doi:10.5194/gmd-2019-378.
32. Ribes, A. & Terray, L. Application of regularised optimal fingerprinting to attribution. Part II: Application to global near-surface temperature. *Clim. Dyn.* **41**, 2837–2853 (2013).
33. Gillett, N. P., Arora, V. K., Matthews, D. & Allen, M. R. Constraining the ratio of global warming to cumulative CO₂ emissions using CMIP5 simulations. *J. Clim.* **26**, 6844–6858 (2013).
34. Jones, G. S., Stott, P. A. & Christidis, N. Attribution of observed historical near-surface temperature variations to anthropogenic and natural causes using CMIP5 simulations. *J.*

Geophys. Res. Atmos. **118**, 4001–4024 (2013).

35. Ribes, A., Planton, S. & Terray, L. Application of regularised optimal fingerprinting to attribution. Part I: method, properties and idealised analysis. *Clim. Dyn.* **41**, 2817–2836 (2013).
36. Shiogama, H. *et al.* Predicting future uncertainty constraints on global warming projections. *Sci. Rep.* (2016) doi:10.1038/srep18903.
37. Annan, J. D. & Hargreaves, J. C. Reliability of the CMIP3 ensemble. *Geophys. Res. Lett.* (2010) doi:10.1029/2009GL041994.
38. Haustein, K. *et al.* A real-time Global Warming Index. *Sci. Rep.* (2017) doi:10.1038/s41598-017-14828-5.
39. Zelinka, M. D. *et al.* Causes of Higher Climate Sensitivity in CMIP6 Models. *Geophys. Res. Lett.* (2020) doi:10.1029/2019GL085782.
40. Tokarska, K. B. *et al.* Past warming trend constrains future warming in CMIP6 models. *Sci. Adv.* (2020) doi:10.1126/sciadv.aaz9549.
41. Liang, Y., Gillett, N. P. & Monahan, A. H. Climate model projections of 21st century global warming constrained using the observed warming trend. *Geophys. Res. Lett.* (2020) doi:10.1029/2019GL086757.
42. Eyring, V. *et al.* ESMValTool (v1.0)-a community diagnostic and performance metrics tool for routine evaluation of Earth system models in CMIP. *Geosci. Model Dev.* (2016) doi:10.5194/gmd-9-1747-2016.
43. Kirchmeier-Young, M. C., Zwiers, F. W. & Gillett, N. P. Attribution of extreme events in Arctic Sea ice extent. *J. Clim.* **30**, 553–571 (2017).
44. Parsons, L. A., Brennan, M. K., Wills, R. C. J. & Proistosescu, C. Magnitudes and Spatial Patterns of Interdecadal Temperature Variability in CMIP6. *Geophys. Res. Lett.* (2020) doi:10.1029/2019GL086588.

	Two-way regression		Three-way regression		
	ANT	NAT	GHG	AER	NAT
Main analysis	0.92 – 1.30	-0.02 – 0.05	1.16 – 1.95	-0.73 – -0.14	-0.01 – 0.06
hist-GHG			1.06 – 1.94	-0.71 – -0.03	-0.01 – 0.07
Hemispheric	0.94 – 1.29	-0.02 – 0.04	1.36 – 2.04	-0.84 – -0.29	-0.02 – 0.05
GISTEMP	1.04 – 1.42	-0.05 – 0.02	1.34 – 2.12	-0.78 – -0.19	-0.04 – 0.03
NOAA	1.02 – 1.39	-0.03 – 0.05	1.37 – 2.15	-0.85 – -0.25	-0.05 – 0.05
GMST	0.80 – 1.10	-0.02 – 0.04	1.04 – 1.69	-0.65 – -0.14	-0.01 – 0.04

501

502

503

504

505

506

507

508

509

510

511

512

Table 1 Multi-model estimates of attributable temperature change between 1850–1900 and 2010–2019 in °C. The table shows 5–95% confidence ranges in attributable warming from the main multi-model analysis (first row), from an equivalent analysis in which the GHG signal is derived from hist-GHG, and the AER signal is derived from historical-ssp245 minus hist-GHG minus hist-NAT (in this case ozone and land-use change are grouped with AER instead of GHG) (second row), from an analysis identical to the main analysis except using 5-yr mean Northern and Southern Hemispheric mean temperature instead of GMST (third row), from analyses identical to the main analysis, except using GISTEMP (fourth row), and NOAAGlobalTemp (fifth row) in place of HadCRUT4, and from an analysis identical to the main analysis, except for HadCRUT4-masked GMST instead of globally-complete GSAT (sixth row).

Figure 1: Comparison of 1850–2019 global mean temperature evolution in observations and CMIP6 simulations. Coloured lines in the top panel show HadCRUT4-masked blended GMST⁵ anomalies relative to the 1850–1900 base period in one historical-ssp245 simulation from each model. The thick brown line shows the multi-model mean, using all ensemble members, but with equal weights given to each model. The thick red line shows the corresponding multi-model mean of globally-complete GSAT. The thick black line shows HadCRUT4¹¹. The lower panel compares HadCRUT4 GMST with simulated GMST from CMIP6 historical-ssp245 simulations with anthropogenic and natural forcings, natural forcing simulations, well-mixed greenhouse gas only simulations, and aerosol only simulations. The multi-model mean and 5–95% ensemble range are shown, both calculated with equal weight given to each model.

Figure 2: Results of a regression analysis applied to CMIP6 models. The left column shows the results of a two-way regression of observed 5-year mean GMST onto the simulated response to anthropogenic (ANT) and natural (NAT) forcings from each model individually, and the right column shows the results of a corresponding three-way regression of observations onto the simulated response to aerosols (AER), natural forcings (NAT) and well-mixed greenhouse gases, ozone and land-use change (GHG). The top row shows regression coefficients and their 5–95% confidence ranges. Regression coefficients inconsistent with zero indicate a detectable response to the corresponding forcing, and regression coefficients consistent with one indicate a consistent magnitude of response in model and observations. The middle row shows the *p*-value resulting from a residual consistency test³⁵. The bottom row shows the 2010–2019 change in global mean near-surface air temperature relative to 1850–1900 attributable to each forcing (5–95% confidence ranges). The horizontal black line indicates an estimate of the observed change in GSAT based on HadCRUT4.

Figure 3: Imperfect model test of multi-model attributable warming calculation. The *x*-axis shows the simulated ensemble mean 2010–2019 temperature change relative to 1850–1900 in response to aerosols only (hist-aer simulations) (blue), natural forcings only (hist-nat simulations) (green) and greenhouse gases, ozone and land-use change (historical-ssp245 minus hist-nat and hist-aer) (grey) in each of the thirteen models used. Each historical simulation from the corresponding model was in turn treated as pseudo-observations, and the remaining twelve models were together used to provide estimates of response patterns to aerosols, natural, and greenhouse gas forcing in an optimal regression. The estimated attributable warming is shown on the *y*-axis. Crosses show best estimates, and vertical bars show 90% confidence ranges. For models with more than one historical-ssp245 simulation, confidence bars are offset along the *x*-axis, to make them visible.

Extended Data Figure 1: Global mean surface temperature (GMST) anomalies in all DAMIP historical simulations. The multi-model mean and 5–95% ensemble ranges, based on all available simulations with equal weight given to each model, are shown. HadCRUT4 GMST is shown in black on the top graph.

Extended Data Figure 2: Results of a regression in which observed changes are decomposed into the response to natural forcings, well-mixed greenhouse gases, and other anthropogenic forcings. As Figure 2, except that the right panels show the results of a three-way regression of observations onto the simulated response to natural forcings (NAT), well-mixed greenhouse gases only (GHG), and other anthropogenic forcings (OTH), consisting of aerosols, ozone and land-use change. In this figure ozone and land-use change are grouped with aerosols, instead of with well-mixed greenhouse gases, as in Figure 2.

Extended Data Figure 3: Regression results based on GISTEMP. As Figure 2, except using GISTEMP in place of HadCRUT4.

Extended Data Figure 4: Regression results based on NOAAGlobalTemp. As Figure 2, except using NOAAGlobalTemp in place of HadCRUT4.

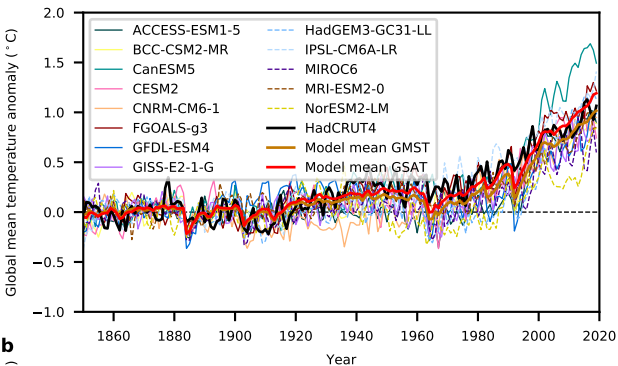
Extended Data Figure 5: Regression results based on hemispheric means. As Figure 2, except using 5-yr mean hemispheric means in place of 5-yr mean GMST in the regressions.

Extended Data Figure 6: Regression coefficients derived using each of the 100 ensemble members of HadCRUT4¹¹. Results are shown for two-way (a) and three-way (b) multi-model regression analyses, as shown in Figure 2a and b, except using each of the 100 members of the HadCRUT4 ensemble dataset in turn.

Extended Data Figure 7: The ratio of 2010–2019 warming relative to 1850–1900 in GSAT to HadCRUT4-masked GMST and globally-complete GMST. The ratio of changes in GSAT to HadCRUT4-masked GMST is shown in (a), and the ratio of changes in GSAT to globally-complete GMST is shown in (b) for each individual historical-ssp245 simulation of each model.

Extended Data Figure 8: Comparison of uncertainty calculation approaches. As Figures 2e and f, except that in each case uncertainties in attributable temperature change are calculated in two ways. Bars show confidence intervals calculated, as in the main analysis, accounting for uncertainty in the ensemble mean simulated 2010–2019 GSAT changes in the case of the individual model analyses, and accounting for uncertainties in the ratio of GSAT to GMST and observational uncertainty, in the case of the multi-model analysis. Horizontal ticks show confidence ranges neglecting these sources of uncertainty. The latter calculation corresponds to

591 multiplying the 5–95% confidence range on the regression coefficient by the corresponding
592 ensemble mean simulated 2010–2019 GSAT change.

a**b**